RSC Advances

PAPER

View Article Online
View Journal | View Issue

Check for updates

Cite this: *RSC Adv.*, 2023, **13**, 15843

Received 4th April 2023
Accepted 18th May 2023

DOI: 10.1039/d3ra02230g

rsc.li/rsc-advances

In situ oxidized TiO_2/MXene ultrafiltration membrane with photocatalytic self-cleaning and antibacterial properties†

Shunkai Xu,‡[ab] Changrong Zhao,‡[a] Guangchao Li,*[a] Zhou Shi[a] and Bin Liu*[a]

Self-cleaning, antimicrobial ultrafiltration membranes are urgently needed to alleviate the low flux problems caused by membrane fouling in water treatment processes. In this study, *in situ* generated nano-TiO_2 MXene lamellar materials were synthesized and then 2D membranes were fabricated using vacuum filtration. The presence of nano TiO_2 particles as an interlayer support layer widened the interlayer channels, and also improved the membrane permeability. The TiO_2/MXene composite on the surface also showed an excellent photocatalytic property, resulting in enhanced self-cleaning properties and improved long-term membrane operational stability. The best overall performance of the TiO_2/MXene membrane at 0.24 mg cm^{-2} loading was optimal, with 87.9% retention and 211.5 L m^{-2} h^{-1} bar^{-1} flux at a filtration of 1.0 g L^{-1} bovine serum albumin solution. Noticeably, the TiO_2/MXene membranes showed a very high flux recovery under UV irradiation with a flux recovery ratio (FRR) of 80% as compared to the non-photocatalytic MXene membranes. Moreover, the TiO_2/MXene membranes demonstrated over 95% resistance against *E. coli*. And the XDLVO theory also showed that the loading of TiO_2/MXene slowed down the fouling of the membrane surface by protein-based contaminants.

1. Introduction

Membrane-based water treatment has become a common technology to address the water pollution issue due to its eco-friendly and sustainable behavior.[1] However, organic contaminants, especially the hydrophobic fractions, can cause severe membrane fouling by adhesion onto the membrane surface during water treatment applications.[2,3] As a result, it inevitably triggers membrane flux loss, high energy consumption and short service lifespan, which has turned up as the Achilles' Heel for the development of membrane technology.[4]

To date, extensive efforts have been paid on suppressing membrane fouling based on the passive reduction of interfacial contaminant adhesion rates.[5–8] To address this root cause of membrane fouling, active antifouling methods (*i.e.*, catalysis) are gaining increasing attentions in recent years. Photocatalysis, being an effective and green method, has emerged as one of the most promising technologies for controlling membrane fouling.[9] In this aspect, various materials and preparation techniques have been adopted to endow membrane with photocatalytic capability. For example, TiO_2-modified membrane prepared by depositing TiO_2 on flat alumina membranes by magnetron sputtering showed a significant capability of degrading methylene blue under UV light.[10] Similarly, Zhang *et al.*[11] successfully deposited N elements into the TiO_2 lattice by atomic layer deposition to prepare membrane materials that can successfully mitigate the bovine serum albumin (BSA) fouling under visible light. Zhang *et al.*[12] successfully prepared photocatalytic graphite oxide/M88A nanofiber membranes with photo-Fenton self-cleaning properties, possessing ultrahigh water flux and photocatalytic activity by ultrasonic-assisted low-temperature hydrothermal synthesis.

In recent years, MXene materials have been used in membrane fabrication due to their unique two-dimensional structure and photocatalytic performance.[13–15] MXene is usually synthesized from corresponding MAX phase with the general formula $M_{n+1}X_nT_x$, where M stands for an early transition metal such as Ti, Nb, V, *etc.*, X stands for C or N and n is typically 1–4, by selective etching of the main group elements A (Al, Ca, *etc.*) to form terminal T_x on the surface (O, F, Cl, *etc.*).[16,17] First MXene membrane with a thickness of 1.5 μm was prepared by Yury Gogotsi *et al.*[18] in 2015. Lin *et al.*[19] also prepared composite membranes by combining N–$Bi_2O_2CO_3$ with MXene to obtain excellent photocatalytic activity and permeability. However, it was observed that the MXene membrane material itself does not possess photocatalytic ability, but highly compatible when compounded with other materials.

---

[a] *Hunan Engineering Research Center of Water Security Technology and Application, College of Civil Engineering, Hunan University, Changsha 410082, PR China. E-mail: lgc_hnu@hnu.edu.cn; ahxclb@163.com*

[b] *Beijing General Municipal Engineering Design & Research Institute Co., Ltd, Beijing 100081, China*

† Electronic supplementary information (ESI) available. See DOI: https://doi.org/10.1039/d3ra02230g

‡ These authors contributed equally to this work.

Integrating MXene with other materials for photocatalysis may affect the structure stability because of the complicated synthesis processes. In contrast, MXene can successfully generate TiO_2 with high photocatalytic properties directly on the surface.[20] Huang *et al.*[21] synthesized nitrogen-doped TiO_2/MXene by mixing melamine in a tube furnace under the protection of CO_2, resulting into an efficient degradation of phenol. The hydrothermal reaction by mixing different concentrations of $NaBF_4$ with Ti_3C_2 can also synthesize TiO_2/MXene materials with excellent perfluorooctanoic acid removal capacity.[22] Unlike conventional photocatalysts, TiO_2 could be *in situ* generated on the MXene surface, ensuring effective dispersion and stable particle size,[23] which enhanced the photocatalytic effect due to the absorbance of photogenerated electrons on MXene matrix.[24] These findings allow the *in situ* oxidation of MXene as a two-dimensional material photocatalyst and its integration in the field of membrane treatment.

In this study, photocatalytic self-cleaning ultrafiltration membranes with TiO_2/MXene were successfully prepared. Firstly, a TiO_2/MXene nanosheet composite material with TiO_2 nanoparticles generated on the surface was prepared by *in situ* oxidation of MXene using a hydrothermal method. After that, TiO_2/MXene ultrafiltration membranes with different loadings were prepared by vacuum filtration. The membrane material with the optimal loading of TiO_2/MXene was selected by filtration experiments with bovine serum albumin (BSA) as model foulant and also tested for self-cleaning behavior. Meanwhile, the antibacterial performance of MXene and TiO_2/MXene materials were also compared, and the mechanism of improving anti-fouling performance of the membrane materials was analyzed by XDLVO theory.

2. Materials and methods

2.1 Materials

The commercial polyvinylidene fluoride (PVDF) membranes (0.22 μm) were purchased from Jinteng, Tianjin, China. Hydrochloric acid (HCl), lithium fluoride (LiF), phosphate-buffered saline (PBS) solution, and BSA were provided by Wanqing, Nanjing, China. The antibacterial properties of the membranes were investigated using *E. coli* previously isolated and purified in the laboratory as a model.

2.2 Preparation of monolayer MXene

The single-layer MXene material was prepared by selective etching of the Al layer in the MAX phase (Ti_3AlC_2).[25] The solution was sealed with plastic wrap and placed on a constant temperature electromagnetic stirrer at 40 °C and stirred for 15 min at 500–600 rpm to completely dissolve the LiF into the concentrated HCl. 2 g of MAX material was added to the solution slowly to prevent spattering. The solution was re-sealed and stirred for 48 h at 500–600 rpm on an induction stirrer at 40 °C. Subsequently, the solution was poured into a 50 mL centrifuge tube and centrifuged at 3500 rpm for 5 min. Acidic washing with 1 M HCl was employed to remove residual LiF. After the acidic washing, centrifugation was repeated with deionized (DI) water until the pH of the supernatant reached 6.0. Finally, the centrifuged precipitate and supernatant were filtered onto a 0.22 μm PVDF membrane to obtain organ-shaped multilayers of Ti_3C_2.

To further prepare the monolayer Ti_3C_2 material, the precipitate that had been filtered onto the membrane was placed back into a centrifuge tube, 45 mL of DI water was added and filled with nitrogen gas for 2 min to remove the oxygen from the liquid. The tube was placed in an ultrasonic cleaner and shaken for 1 h. Shake the centrifuge tube by hand every 10 min to ensure the material did not sink and ice was added to the ultrasonic cleaner to keep the temperature below 30 °C. After shaking, the solution was centrifuged for 30 min at 3500 rpm, and the supernatant was then termed as the Ti_3C_2 monolayer solution. This monolayer solution was placed directly in a freeze dryer and the obtained powder was stored in a small bottle protected by inert gas in a 4 °C refrigerator.

2.3 Preparation of monolayer TiO_2/MXene

100 mg of monolayer MXene (Ti_3C_2) was dissolved in 20 mL of DI water and placed in an ultrasonic cleaner for 10 min. The solution was then placed in a 50 mL hydrothermal kettle and heated at 120 °C for 24 h to produce a monolayer TiO_2/MXene solution. The prepared solution was poured into a 50 mL centrifuge tube, flushed with nitrogen gas to remove the air from the solution, and then stored in a sealed refrigerator at 4 ° C. Before the experiment, 5 mL of the solution was placed in a small beaker that had been weighed, then transferred to a 70 ° C oven for drying, and then weighed again to calculate the concentration of the solution.

2.4 Preparation of ultrafiltration membranes

A commercial PVDF membrane with a pore size of 0.22 μm was used as the support and the desired two-dimensional membrane material was prepared by a vacuum-assisted filtration (the effective modification area was 12.56 cm^2) method. Prior to filtration, a 0.02 mg mL^{-1} colloidal solution was prepared by adding DI water into the as-prepared monolayer TiO_2/MXene solution with known concentration. Then, 50 mL, 100 mL, 150 mL, and 200 mL of TiO_2/MXene and MXene colloidal solutions were filtered separately under vacuum to produce the 2D layered TiO_2/MXene membranes. According to the increase of load, MXene loaded membranes are named M-0.08 (0.08 mg cm^{-2}), M-0.16 (0.16 mg cm^{-2}). M-0.24 (0.24 mg cm^{-2}), and M-0.32 (0.32 mg cm^{-2}). TiO2/MXene loaded membranes are named TM-0.08 (0.08 mg cm^{-2}), TM-0.16 (0.16 mg cm^{-2}), TM-0.24 (0.24 mg cm^{-2}), TM-0.32 (0.32 mg cm^{-2}). A commercially available PVDF ultrafiltration membrane (100 kDa, Depo) was used as the benchmark. A schematic diagram of the preparation is shown in Fig. S1.†

2.5 Characterization

Scanning electron microscopy (SEM, Quanta FEG 250, FEI, USA) was utilized for observing the cross-sectional morphologies of 2D material membranes. The membrane surface roughness was analyzed by using atomic force microscopy (AFM, Dimension

Icon, Bruker, Germany). The hydrophilicity of the membrane material was determined by contact angle determination (OCA 20, dataphysics, Germany) with three different solutions (water, glycerol, diiodomethane). The zeta potential values of the membranes were measured with a solid-state zeta potential analyzer (Surpass, Anton Paar, Austria), and the charge properties of BSA were determined by a zeta potential analyzer (Nano S90, Malvern, UK). The crystallinity of the material was measured by X-ray diffraction (XRD, SmartLabXE, Rigaku, Japan) and the nanosheet spacing of the 2D material was determined by small-angle diffraction. X-ray photoelectron spectroscopy (XPS, ESCALAB 250Xi, Thermo SCIENTIFIC, USA) was used to analyze the relative abundance of functional groups of MXene material before and after hydrothermal process/reaction. The signals were measured with an EPR spectrometer (ER200-SRC, Bruker, GER).

2.6 Membrane flux and photocatalytic recovery test

Dead end filtration setup was utilized to measure the membrane flux. The effective membrane area was 12.56 cm^2, and the operating pressure was 1 bar. The whole process was divided into four stages: (1) pure water filtration to determine the initial membrane flux, (2) filtration with 1.0 g L^{-1} of BSA solution for 45 min, (3) fouled membranes were placed under UV light (36 W, 365 nm) for 6 h, (4) membranes were filtered again using 1.0 g L^{-1} of BSA solution for 30 min. The filtration protocol was conducted in triplicate. During the experiment, the Bradford method was chosen to determine the concentration of BSA solution at 595 nm to obtain the retention rate of the membrane, taking into account the properties of the Komas Brilliant Blue solution such as protein binding discoloration. The formula was calculated as eqn (1)

$$\text{Rejection ratio} = \frac{C_0 - C_1}{C_0} \times 100\% \tag{1}$$

where C_0 and C_1 are the concentrations of the BSA solution before and after filtration, respectively.

The flux recovery ratio (FRR) is used to evaluate the self-cleaning properties of the membrane. The formula is calculated as eqn (2)

$$\text{FRR} = \frac{J_1}{J_0} \times 100\% \tag{2}$$

where J_1 represents the water flux after UV irradiation and J_0 represents the original water flux.

2.7 EEM test

Excitation emission matrix (EEM) were measured using a fluorescence spectrophotometer (F-320, Jiangdong Technology, China). The Yangtze River water was selected as the real water sample for the separation performance of the modified membrane. The Yangtze River water was first passed through a 0.22 μm membrane and then stored in a 4 °C refrigerator. For the membrane permeation experiments, the pretreated river water was filtrated and the permeation was collected. The fluorescence was scanned at a speed of 12 000 nm min^{-1} in the wavelength range of (EX, EM) = (200–500 nm, 200–600 nm), with a slit width of 5 nm and a photomultiplier voltage of 700 V.

2.8 Antibacterial ability of the membrane

E. coli was cultured in Luria–Bertani (LB) medium at 36 °C. Further passages were cultured in 1 mL of overnight cell suspension, and the cells form exponential growth phase were taken after 12 h. *E. coli* cultures were centrifuged at 4500 rpm for 5 min and the sediment was washed thrice with phosphate-buffered saline (PBS) solution. The cell pellet collected after centrifugation was resuspended in PBS and diluted to a cell concentration of approximately 2 × 10^3 CFU mL^{-1}. The antibacterial capacity of the PVDF support, MXene, and TiO_2/MXene membranes was determined by passing the *E. coli* suspension through the membrane by filtration.[26,27] The filtration components and all glassware used were autoclaved prior to each experiment. Membrane samples (including controls) were sterilized in a 75% v/v ethanol solution, air-dried and UV irradiated for 30 minutes prior to filtration. 50 μL of bacterial suspension (2 × 10^3 CFU mL^{-1}) was further diluted to 10 mL of solution in PBS and aspirated through PVDF, MXene, and TiO_2/MXene membranes. The bacterially treated membranes were plated on LB agar plates and incubated under visible light irradiation/dark conditions at a controlled temperature of 37 °C for 24 h. The light source is a 400–800 nm wavelength LED light source with 10 W power, 20 cm away from the LB agar plates. A black plastic bag was placed over the LB agar plates to isolate the light source to represent the dark state. Finally, the growth of colonies on the membrane surface was observed and the number of colonies grown were counted to quantify the bactericidal effect of the membranes.[28] The viability of the bacterial cells on the membrane was determined using the colony counting method. Each experiment was repeated five times and the results were represented by box plots.

After the experiment, the microbial morphology of the membrane surface was determined using SEM. The samples were prepared by removing the incubated membranes with forceps and fixing the microorganisms on the surface with 2.5% glutaraldehyde at 4 °C for 4 h, then washing twice with 0.1 M phosphate buffer solution (pH = 7.4). The membranes were dehydrated with ethanol (20, 40, 60, 80, 100%) for 10 min each time, then replaced with an ethanol-*tert*-butanol (1 : 1, v/v) solution for 20 min, followed by 100% *tert*-butanol for 20 minutes and dried completely at room temperature.

2.9 XDLVO theory

The XDLVO theory can assess the surface interaction energy between the membrane and foulants through zeta potential and contact angle, thus explaining the adhesion behavior of the contaminants towards the membrane surface.[29] According to XDLVO theory, the total interfacial interaction force between the membrane and the foulant (U^{TOT}) is derived from the accumulation of the following three interaction energy vectors.

$$U^{\mathrm{TOT}} = U^{\mathrm{LW}} + U^{\mathrm{AB}} + U^{\mathrm{EL}} \tag{3}$$

where U^{TOT} is the total interaction energy, U^{LW}, U^{AB}, and U^{EL} are van der Waals interaction (LW), acid–base interaction (AB), and electrostatic interaction (EL), respectively. These three interaction energies can be expressed as.

$$U^{\mathrm{LW}} = 2\pi\Delta G_{h_0}^{\mathrm{LW}}\frac{{h_0}^2 a}{h} \tag{4}$$

$$U^{\mathrm{AB}} = 2\pi a\lambda\Delta G_{h_0}^{\mathrm{AB}}\exp\left(\frac{h_0 - h}{\lambda}\right) \tag{5}$$

where a is the particle radius (unit) of the foulant, h is the distance between the two planes of interaction, and h_0 (=0.158 nm) is the minimum distance. λ (=0.6 nm) is the decay length of the polar interaction force in an aqueous solution. $\Delta G_{h_0}^{\mathrm{LW}}$ and $\Delta G_{h_0}^{\mathrm{AB}}$ are the LW, AB interface action energy components at the minimum distance h_0, respectively. The equations are as follows.

$$\Delta G_{h_0}^{\mathrm{LW}} = 2\left(\sqrt{\gamma_{\mathrm{w}}^{\mathrm{LW}}} - \sqrt{\gamma_{\mathrm{m}}^{\mathrm{LW}}}\right)\left(\sqrt{\gamma_{\mathrm{f}}^{\mathrm{LW}}} - \sqrt{\gamma_{\mathrm{w}}^{\mathrm{LW}}}\right) \tag{6}$$

$$\Delta G_{h_0}^{\mathrm{AB}} = 2\sqrt{\gamma_{\mathrm{w}}^{+}}\left(\sqrt{\gamma_{\mathrm{m}}^{-}} + \sqrt{\gamma_{\mathrm{f}}^{-}} - \sqrt{\gamma_{\mathrm{w}}^{-}}\right) + 2\sqrt{\gamma_{\mathrm{w}}^{-}}\left(\sqrt{\gamma_{\mathrm{m}}^{+}} + \sqrt{\gamma_{\mathrm{f}}^{+}} - \sqrt{\gamma_{\mathrm{w}}^{+}}\right) - 2\left(\sqrt{\gamma_{\mathrm{m}}^{+}\gamma_{\mathrm{f}}^{-}} + \sqrt{\gamma_{\mathrm{m}}^{-}\gamma_{\mathrm{f}}^{+}}\right) \tag{7}$$

where γ^{LW} is the LW surface tension sub term, γ^{+}, and γ^{-} represent the electron donor and electron acceptor parameters, and the subscripts w, m, and f represent water, membrane, and contaminants, respectively. After determining the contact angles of the membrane and contaminants utilizing the three known surface tension parameter, the extended Young's equation[30] was derived for all parameters. The extended Young's equation is as follows.

$$(1 + \cos\theta)\gamma_{\mathrm{l}}^{\mathrm{TOT}} = 2\left(\sqrt{\gamma_{\mathrm{s}}^{\mathrm{LW}}\gamma_{\mathrm{l}}^{\mathrm{LW}}} + \sqrt{\gamma_{\mathrm{s}}^{+}\gamma_{\mathrm{l}}^{-}} + \sqrt{\gamma_{\mathrm{s}}^{-}\gamma_{\mathrm{l}}^{+}}\right) \tag{8}$$

where θ is the contact angle, and γ^{TOT} is the total surface tension, which includes the sum of the LW and AB polar components, where $\gamma^{\mathrm{AB}} = 2\sqrt{\gamma^{+}\gamma^{-}}$ is the polar surface tension component. The subscripts "s" and "l" represents the solid and liquid surfaces, respectively.

The electrostatic interaction energy U^{EL} can be determined from the following equation.

$$U^{\mathrm{EL}} = \pi\varepsilon_{\mathrm{r}}\varepsilon_0 a\left(2\zeta_{\mathrm{f}}\zeta_{\mathrm{m}}\ln\frac{1 + \exp(-\kappa h)}{1 - \exp(-\kappa h)} + \left({\zeta_{\mathrm{f}}}^2 + {\zeta_{\mathrm{m}}}^2\right)\ln(1 - \exp(-2\kappa h))\right) \tag{9}$$

where ε_0 (=8.854 × 10^{-12} $\mathrm{CV^{-1}\,m^{-1}}$) is the vacuum dielectric constant, ε_{r} (=78.5) is the relative dielectric constant of the aqueous solution, ζ_{m} and ζ_{f} are the zeta potentials of the membrane and contaminants, respectively. κ is the inverse of the Debye shielding constant. The specific equations are as follows.

$$\kappa = \sqrt{\frac{e^2\sum n_i {z_i}^2}{\varepsilon_{\mathrm{r}}\varepsilon_0 kT}} \tag{10}$$

where e (=1.6 × 10^{-19} C) is the charge of the electron; n_i is the molar concentration of ion i in the original solution and z_i is the valence of ion i; k is the Boltzmann constant and T is the absolute temperature. The background electrolyte concentration in this study was 0.01 M NaCl and all operations were carried out at room temperature (25 °C).

3. Results and discussion

3.1 Material characterization

The morphology and structural details of the 2D modified material are shown in Fig. 1. The initial MAX phase Ti_3AlC_2 material (Fig. 1a) was successfully exfoliated by etching ultrasonics to produce a single lesser layer of MXene material (Fig. 1b). The TiO_2/MXene sheet layer material was then successfully prepared by the hydrothermal method. After *in situ* hydrothermal treatment, anatase TiO_2 with a lattice spacing of 0.35 nm was generated on the surface of the material[31] (Fig. 1c). The prepared MXene and the hydrothermal TiO_2/MXene materials were diluted up to 0.02 M (Fig. 1d), and found that the solutions showed a light green color, and have an obvious Tyndall effect under infrared laser pointer irradiation before and after hydrothermal treatment. These findings confirmed that the material was well dispersed in the aqueous solution, showing a single/few layer in suspension.[32]

XPS was used to characterize the elemental composition and chemical valence analysis of TiO_2/MXene. Three elements, Ti, O, and C, were selected for the comparison and the resulting data was separated into peaks by XPS Peak software. As shown in Fig. 1e, the Ti 2p3/2 components centered at 456.0, 455.8, 457.4 and 459.3 eV were associated with the Ti–C bonds, Ti–X bonds or sub-stoichiometric TiC_x (x < 1), and the Ti ions with reduced charge states (Ti_xO_y) and Ti^{4+} ions (TiO_2) respectively.[33] Among them, the peak of TiO_2 was found, indicating that a large amount of TiO_2 was generated hydrothermally. Moreover, three peaks of O 1s positioned at 530.9, 532.7, and 534.1 eV (Fig. 1f), were found associated with Ti–O (TiO_2), C–Ti–O_x, and C–Ti–OH_x, respectively. According to Cai *et al.*,[34] the C 1s can be divided into six peaks at 282.2, 283.3, 284.8, 285.5, 284.1, and 289.2 eV, corresponding to the C–Ti, C–Ti–O, C–C, C–OH, C–O, and C–F bonds, respectively. According to the XPS pattern, the C peaks of TiO_2/MXene were mainly assigned to the C–C and C–Ti bonds (Fig. 1g), which also confirms the presence of the Ti_3C_2 structure of the matrix material. And the presence of C–O/C=O bonds indicates that a small portion of C elements were oxidized.

3.2 Membrane characterization

The monolayers of MXene material were loaded onto the PVDF membrane surface by vacuum-assisted filtration to form a dense laminar structure (Fig. 2). In contrast, the nanoscale TiO_2 were generated at the surface of the 2D material after hydrothermal treatment, and the TiO_2 particles grown on the

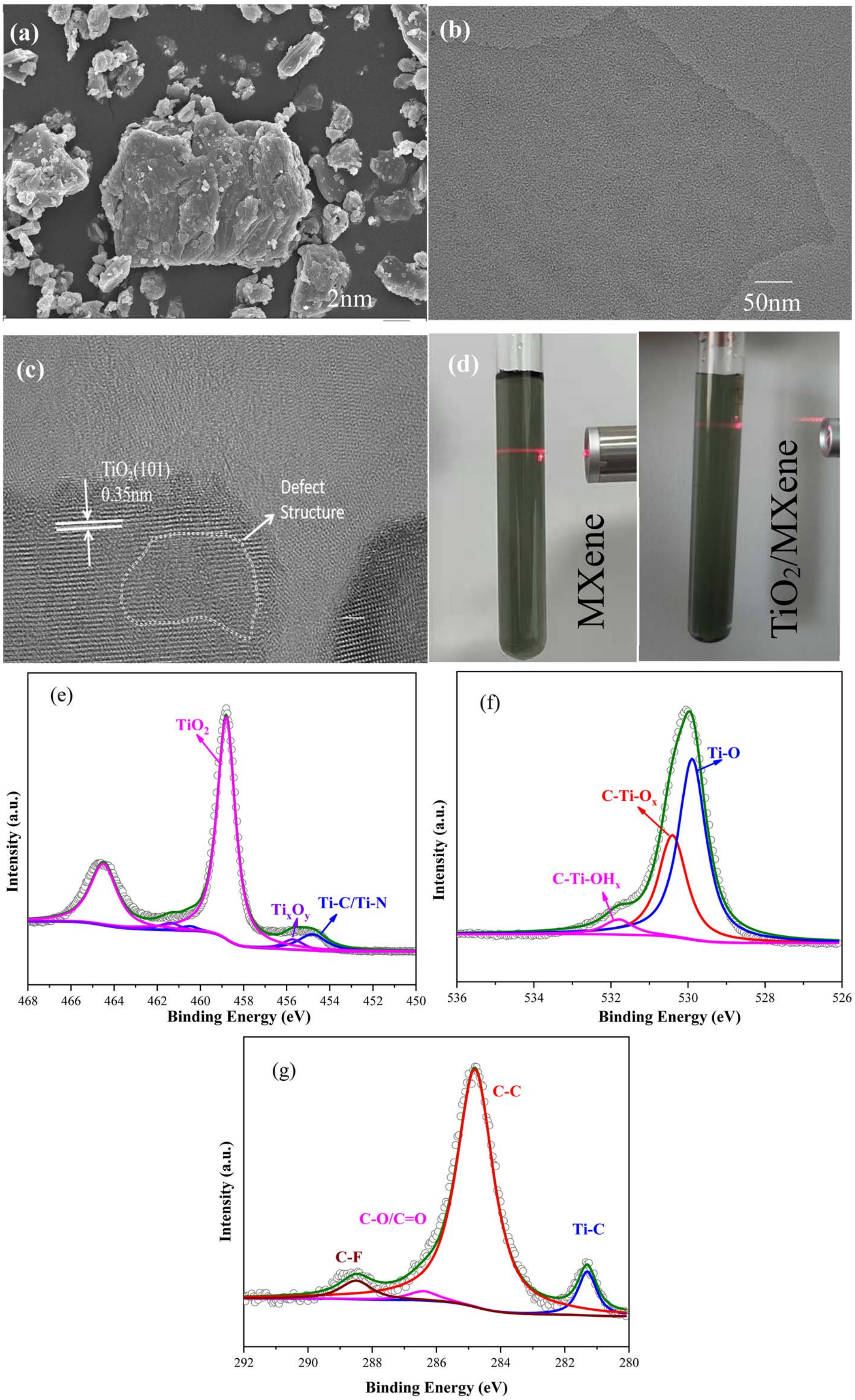

Fig. 1 (a) SEM of MAX material; (b) TEM of monolayer MXene; (c) high resolution TEM of monolayer TiO_2/MXene; (d) Tyndall effect of dilute solution at 0.02 mg mL^{-1}; XPS of (e) Ti 2p, (f) O 1s and (g) C 1s of TiO_2/MXene.

surface of the lamellae were tightly packed in the middle of the lamellae during the vacuum filtration process. Meanwhile, the SEM images also showed that the thicknesses of the modified layers were 496 nm, 728 nm, 952 nm and 1184 nm by increasing the TiO_2/MXene loading from 0.08 mg cm^{-2} to 0.32 mg cm^{-2}. Based on the comparison of the loading thickness of the two materials, combined with the loadings, it can be seen that the MXene material loaded membrane material is more compact, but with the narrow interlayer channels. In contrast, the nanoparticles generated on the surface of TiO2/MXene lamellae

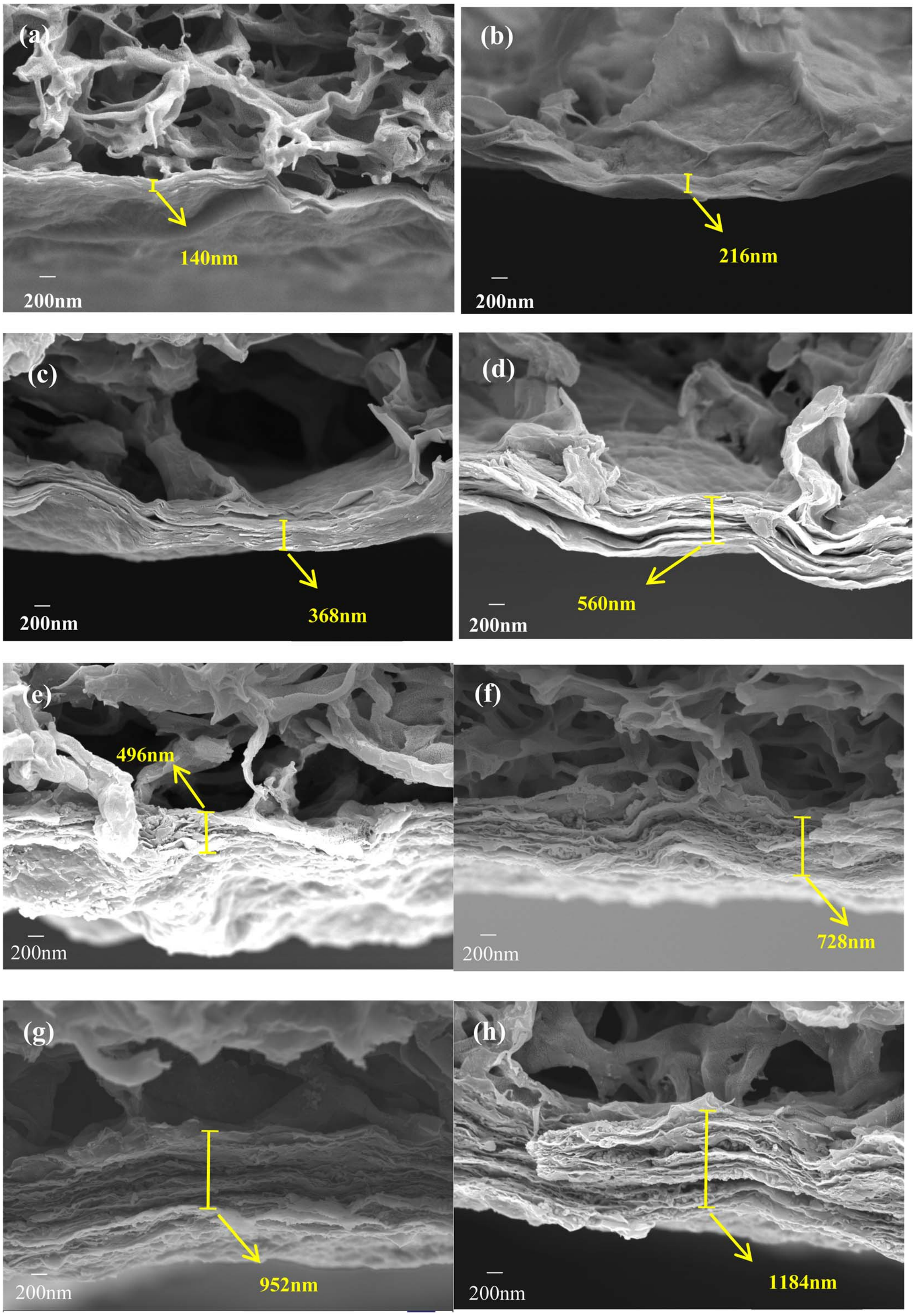

Fig. 2 Cross-sectional SEM image of (a) M-0.08; (b) M-0.16; (c) M-0.24; (d) M-0.32 and (e) TM-0.08; (f) TM-0.16; (g) TM-0.24; (h) TM-0.32.

are supported like pillars between two lamellae close to each other, widening the layer spacing and thus enhancing the flux.

Fig. 3a demonstrates the change of surface hydrophilicity after MXene modification. The addition of the MXene material caused a slight increase in the surface hydrophilicity, as shown by the decrease in water contact angle from 84.9° to 71.5°, due to the inherent hydrophilicity of the MXene material.[35] Moreover, the water contact angle of the TiO_2/MXene membrane

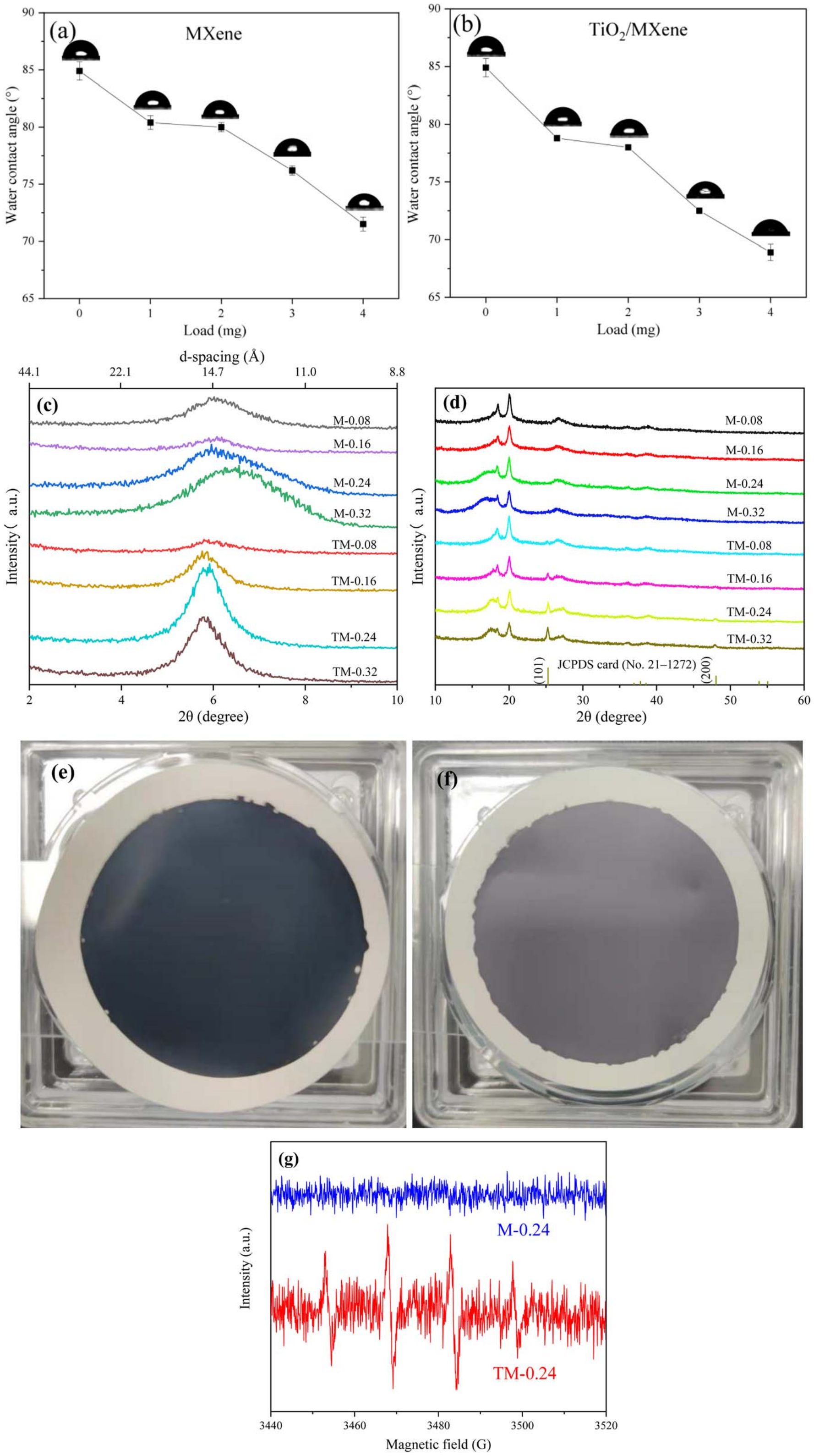

Fig. 3 Water contact angles of (a) MXene and (b) TiO_2/MXene membranes, (c) XRD small-angle diffraction image, (d) XRD image of the eight membranes and pictures of (e) M-0.24, (f) TM-0.24. (g) EPR curves of hydroxyl radicals.

after hydrothermal treatment further decrease up to 68.9° (Fig. 3b). This decrease was attributed to the hydrothermal oxidation, resulting into the production of TiO_2 nanomaterials and some oxygen-containing functional groups on the membrane surface, enhancing the hydrophilicity of the membrane.[36]

XRD analysis was carried out on the membranes (Fig. 3c), the layer spacing size of both MXene (13–14 Å) and TiO_2/MXene membranes (>15 Å) was obtained by using Bragg equation. The layer spacing of TiO_2/MXene membrane was found slightly higher as compared to MXene membrane. This was due to the presence of nano-TiO_2 on the surface of the TiO_2/MXene sheet material, and these nanoparticles were wrapped inside the sheet layer, thus increasing the layer spacing.[37] After hydrothermal treatment, there were still some MXene sheets with only a small amount of TiO_2 on the surface, which endows the robust membrane structure after filtration. Moreover, the XRD images of the TiO_2/MXene membranes also shows new peaks at 25.28° and 48.05° compared to the MXene membranes (Fig. 3d). These news peaks perfectly match with the (101) and (200) planes of the anatase TiO_2 phase (JCPDS 21-1272), indicating the successful preparation of *in situ* grown TiO_2/MXene materials by hydrothermal reaction.

As shown in Fig. 3(e and f), the color of the membrane surface prepared from MXene material was appeared as pure black, while TiO_2/MXene loading on the PVDF membrane showed a grey-black color after naturally drying in air. This phenomenon was credited to the generation of TiO_2 particles on the surface of the MXene nanosheet layer by hydrothermal heat, which slightly diminishes the color depth.[38] Meanwhile, as shown in Fig. 3f, comparing the epr tests of M-0.24 and TM-0.24 under UV light, it was found that no hydroxyl radicals were generated on the surface of the MXene loaded membrane under UV irradiation. And the TiO_2/MXene loading resulted in the ability of photocatalytic generation of strong oxidative hydroxyl radicals under UV irradiation. This demonstrates that the TM-0.24 membrane possesses the potential for photocatalytic self-cleaning.

3.3 Membrane flux, separation, and photocatalytic self-cleaning

Permeability performance was conducted with all modified membranes (Fig. 4a), and it was found that the membrane flux decreased gradually with the increasing loading dosage, irrespective of the material type and treatment performed. The flux of M-0.08 decreased from 528.17 L m^{-2} h^{-1} bar^{-1} to 60.77 L m^{-2} h^{-1} bar^{-1} of M-0.32. Additionally, the TiO_2/MXene membranes also showed the decrease in flux from 791.82 L m^{-2} h^{-1} bar^{-1} of TM-0.08 to 134.92 L m^{-2} h^{-1} bar^{-1} of TM-0.32. This flux decline was due to the massive transport resistance against the increased thickness of the selective layer through which water molecules need to pass as the loading increases. The flux of the TiO_2/MXene membranes was found larger than that of the MXene membrane due to the partial widening of the interlayer channels of the *in situ* generated TiO_2 nanoparticles.

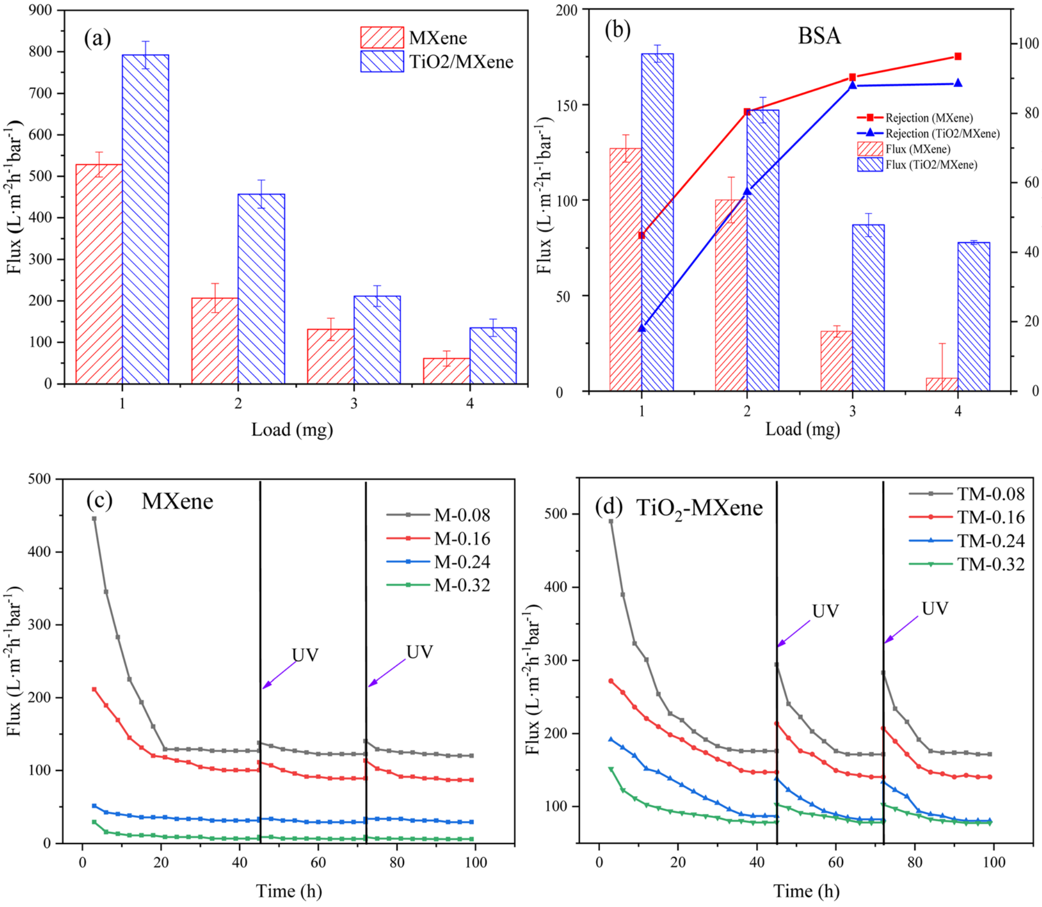

Fig. 4 Membranes (a) pure water flux and (b) BSA retention and stabilization flux, UV self-cleaning ability of (c) MXene and (d) TiO_2/MXene membranes under BSA contamination.

Meanwhile, the production of TiO_2 also resulted in the enhanced hydrophilicity of MXene, which further improves permeability.[39,40]

In contrast, the retention of BSA showed the opposite trends (Fig. 4b), the retention rate of the MXene membrane for BSA was 44.86%, 80.40%, 90.35%, and 96.32% from low to high loadings, respectively. The retention rates of TiO_2/MXene membranes were slightly reduced compared to the MXene membranes because of the increased interlayer spacing caused by hydrothermal treatment, ranging from 17.92% to 88.51%. Combined with the trade off effect, the membrane with 3 mg loading was the optimal group, especially for the TM-0.24.

The fouled membranes were irradiated with UV and the self-cleaning ability was explored by the membrane flux recovery after irradiation. Negligeable recovery in membrane flux was observed after the UV irradiation of MXene membranes (Fig. 4c), with FRR values ranging from 31% to 55%. The limited flux recovery was probably due to the degradation of contaminants caused by the germicidal nature of the UV itself[41] and the small amount of TiO_2 generated by the natural oxidation of the MXene surface.[42] In contrast, the fouled TiO_2/MXene membrane exhibited an extremely high flux recovery through UV irradiation (Fig. 4d), with FRR values in capable of reaching 80%. Such a high self-cleaning performance is not only due to the generation of titanium dioxide particles from nano-anatase. Also, the catalytic performance of the catalyst is enhanced by the presence of MXene substrate, which is able to rapidly trap photogenerated electrons generated by photocatalysis when UV light irradiates TiO_2, preventing the compounding of photogenerated electrons and holes.[43] This indicated that the TiO_2/MXene membrane has a stronger self-cleaning ability than the MXene membrane. Comparing the prepared TM-0.24 membranes with existing self-cleaning ultrafiltration membranes (Table S2†), it can be found that our membranes have higher FRR values under the same pollution conditions while maintaining a much higher flux level than commercially available ultrafiltration membranes. At the same time, the structure and performance of TM-0.24 membranes prepared by vacuum filtration are more stable than the complex membrane preparation process.

We performed EEM analysis of filtered water samples by using a fluorescence spectrophotometer. According to Chen *et al.*[44] the EEM reflects the dynamics of dissolved organic matter (DOM) from aromatic proteins, soluble microbial by-product-like compounds, xanthates and humic acid-like compounds. According to Fig. 5a, it can be concluded that the corresponding interval of fluorescence of DOM in Yangtze water mostly lies between EM/EX – 300 nm/250 nm to EM/EX – 500 nm/400 nm, and there are two peaks in this range. One peak was between EM/EX – 250 nm/250 nm to EM/EX – 375 nm/350 nm, representing fluorescent substances as dissolved cellular production, and another peak was between EM/EX – 375 nm/250 nm to EM/EX – 500 nm/400 nm, representing humic acid-like substances.[45,46]

When we loaded the 2D materials on the PVDF membrane surface, the prepared 2D ultrafiltration membranes were more effective in removing DOM-like substances as the loading of both MXene and TiO_2/MXene materials gradually increased. The performance of the membrane basically reached the best when the loading amount reached 0.24 mg cm^{-2}. As shown in Fig. 5, with the increase of loading, the effect of MXene membrane on the removal of humic substances gradually increased, but the removal efficiency of microbial by-products did not change much. This is because as the loading increases, the number of layers stacked out of the MXene 2D material becomes progressively larger, and the DOM material crossing the membrane needs to pass through defects on the

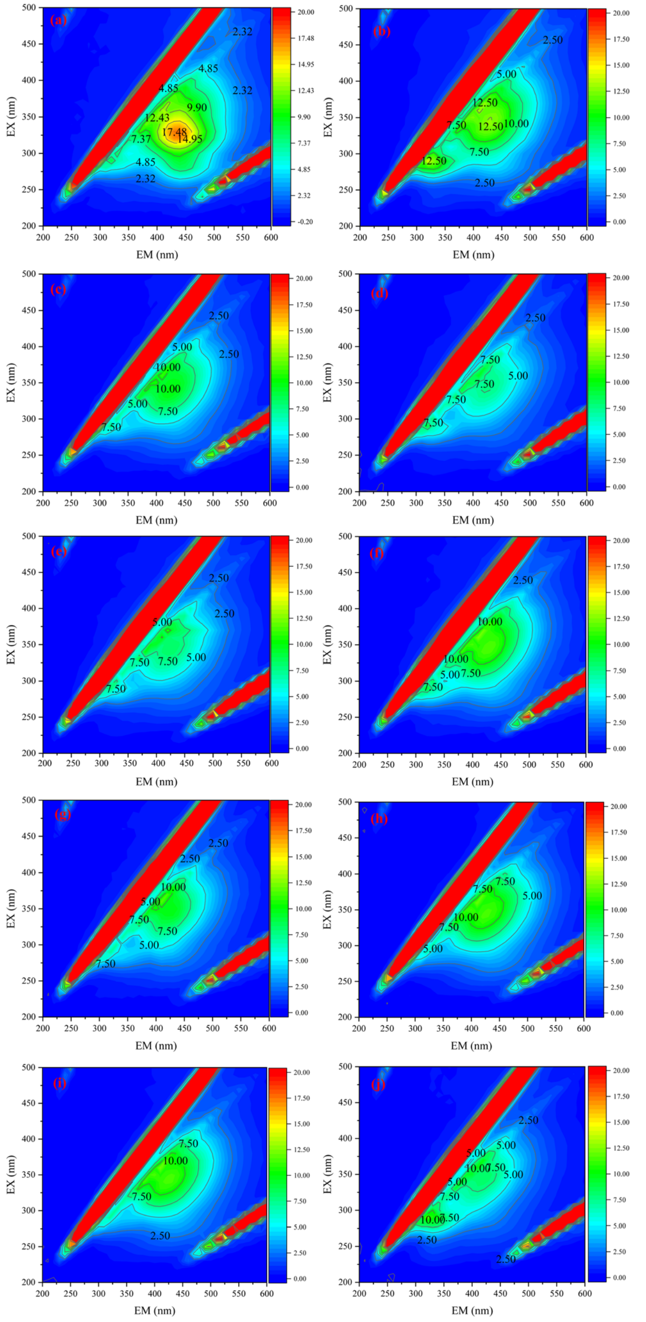

Fig. 5 EEM images of (a) raw water of Yangtze River water and after (b) M-0.08; (c) M-0.16; (d) M-0.24; (e) M-0.32; (f) TM-0.08; (g) TM-0.16; (h) TM-0.24; (i) TM-0.32; (j) commercially available ultrafiltration membrane filter.

surface of the sheet material and be transported within the interlayer channels. In turn, higher loading represents an increase in interlayer channels and a more complete structure. However, most of the soluble microbial by-products are hydrophobic small molecules such as proteins and organic acids, which may pass through the membrane pores with the water flow during the removal process. TiO_2/MXene membranes are significantly more effective in removing soluble microbial by-products than MXene membranes due to their stronger hydrophilic surface properties. Based on the comparison with commercially available ultrafiltration membranes, it can be seen that the 2D laminar modified membranes prepared by our method are more effective in removing dissolved microbial by-products from Yangtze water, with the TiO_2/MXene membrane being more effective. The removal of humic substances was also better with the MXene modified membranes.

3.4 Antibacterial properties

It is well known that the presence of microorganisms in water not only poses a risk to water safety but also act as biological foulant which may further cause flux attenuation. In this study, commercially available ultrafiltration membranes and nano-TiO_2 loaded ultrafiltration membranes were compared with M-0.24 and TM-0.24. The *E. coli* was used as a common model bacterium to assess the anti-microbial contamination activity of the modified membranes. Equal growth of *E. coli* cells was observed after 24 h incubation on different membrane materials (Fig. 6(a–d)), representing the similar behavior of bacterial growth on both PVDF and TiO_2 loaded membranes. Whereas the relatively less bacterial growth was observed on M-0.24 surface, and the TM-0.24 surface showed almost no bacterial community production. As shown in Fig. 6f, The antimicrobial performance of the M-0.24 was slightly improved under light conditions due to the loading of MXene (Fig. 6e).[47,48] The TM-0.24 exhibited over 95% inhibition of *E. coli* growth, regardless of the presence of light illustrating the improved antimicrobial performance due to the production of TiO_2 on the MXene. Two-dimensional materials have an antibacterial mechanism that is mainly caused by the puncture of bacterial cells by sharp and hard edges, resulting in leakage of cell contents. When the flat MXene was prepared into a membrane, the structure of layers stacked up leads to a relatively flat membrane surface. In contrast, when the TiO_2/MXene nanosheets were prepared into membranes, the presence of TiO_2 made the nanosheet stacks no longer flat and the sharp edges were exposed on the surface of membrane. When bacteria attach to the membrane surface, they could be pierced by the sharp edges, leading to cell inactivation.[49,50] The AFM images (Fig. 6g and h) showed the highly rough and sharp surface of the TM-0.24, and these sharp edges can cause cell membrane to be scratched, resulting in cell death.[51] Meanwhile, the rough nanostructured surface can also exert more pressure on the attached cells, causing stress-induced extracellular polymers (EPS) release and cell death by rupture.[52]

To further investigate the interaction between the modified membrane surface and the bacteria, the bacterial communities

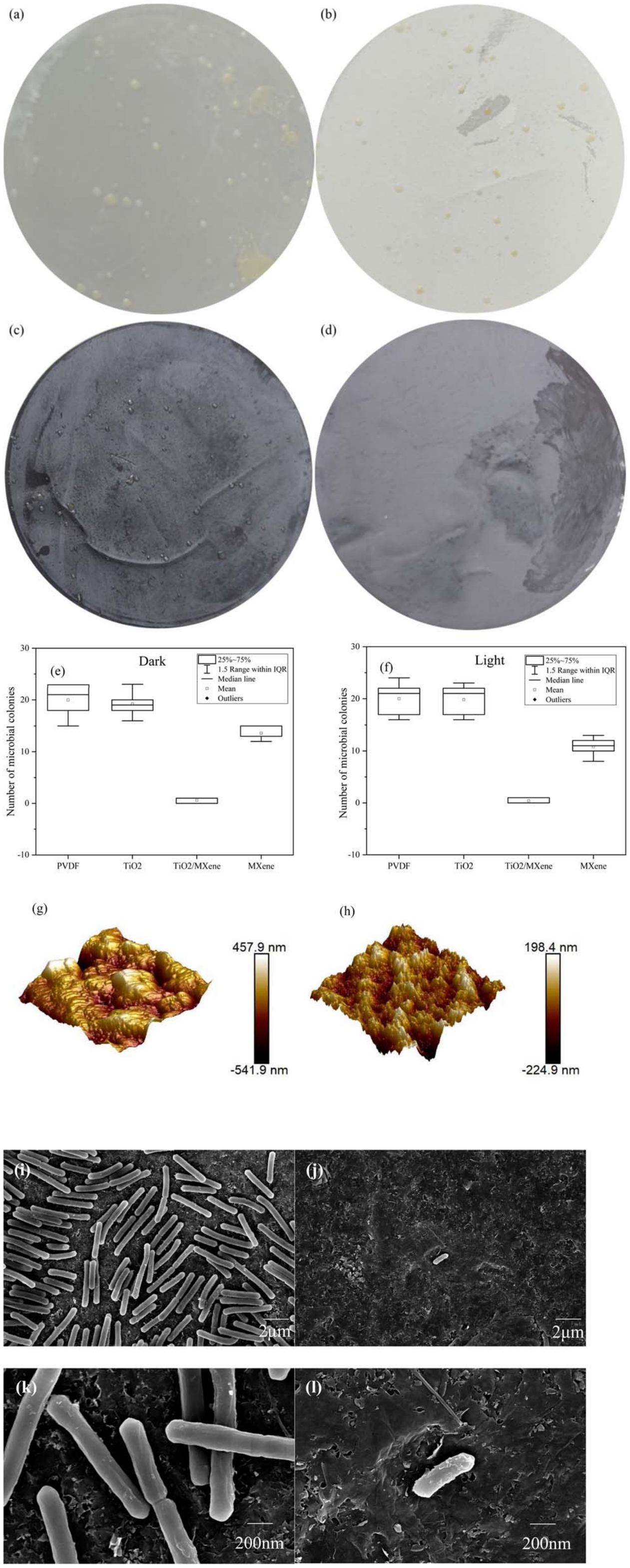

Fig. 6 Microbial growth of (a) PVDF membrane, (b) nano-TiO_2 loaded membrane, (c) M-0.24, (d) TM-0.24, and (e) bacterial growth numbers of the membrane under (e) dark, (f) light conditions, AFM images of (g) M-0.24 and (h) TM-0.24, SEM low magnification images of the *E. coli* colonies grown on (i) M-0.24 and (j) TM-0.24, high magnification images of *E. coli* grown on (k) M-0.24 and (l) TM-0.24.

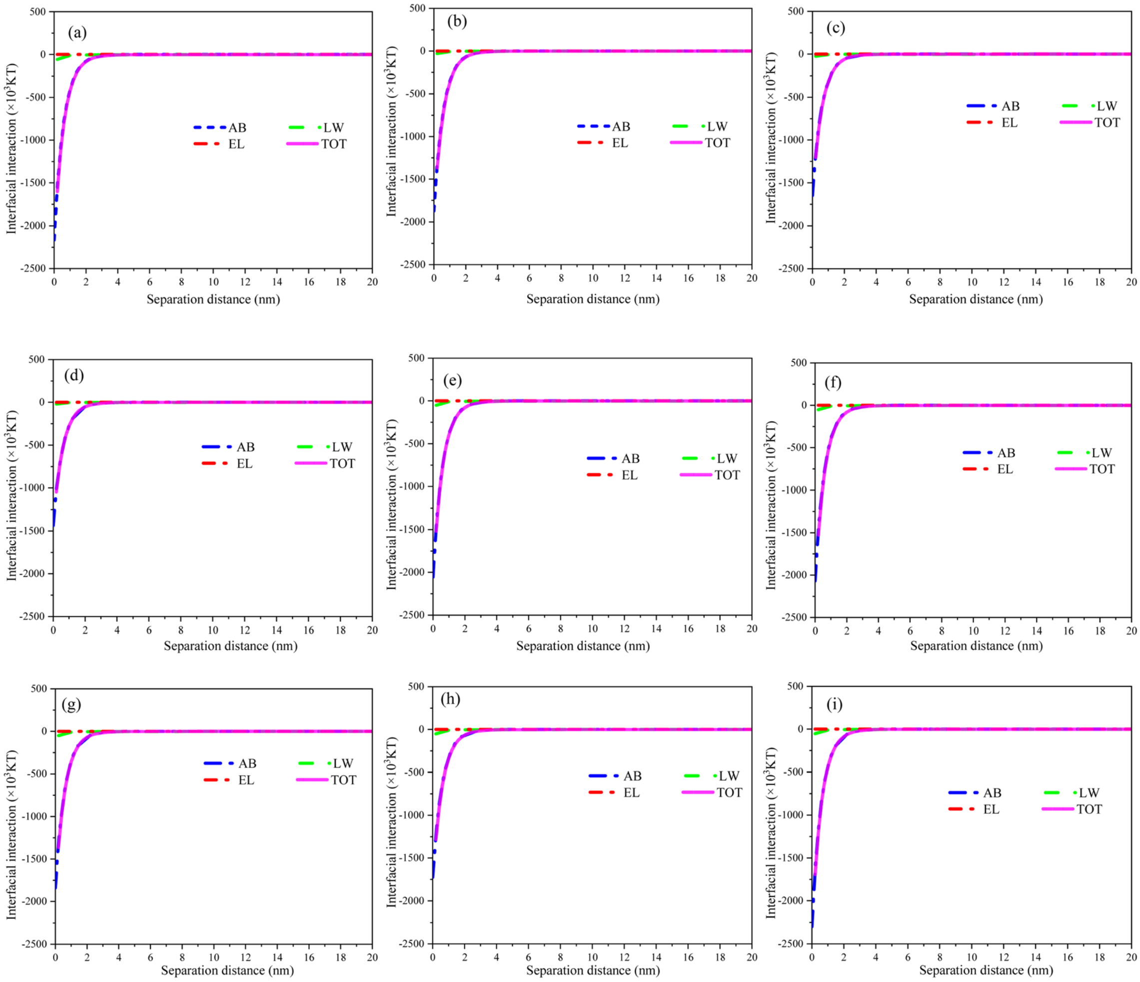

Fig. 7 Interaction energies of (a) M-0.08, (b) M-0.16, (c) M-0.24, (d) M-0.32, (e) TM-0.08, (f) TM-0.16, (g) TM-0.24, (h) TM-0.32; and (i) commercial PVDF ultrafiltration membrane with contaminants (BSA).

on the MXene and TiO_2/MXene surfaces after incubation were also observed. The cell density of bacteria was significantly higher on the M-0.24 surface than the TM-0.24 surface (Fig. 6i and j). Additionally, the bacterial surface on the M-0.24 surface was found to be smooth and structurally intact under high magnification (Fig. 6k and l), however, the bacteria on the TM-0.24 surface had some particles and debris on its rough surface. The presence of these fragments may also cause damage to the cell membrane, which can lead to cell inactivation.[53] Moreover, the *in situ* generated nanoparticles may affect the attachment of microorganisms on the membrane surface.[54] These findings are also consistent with Rasool *et al.*[55] that the aging of MXene in the air could produce TiO_2, thus enhancing the bactericidal effect of the membrane material.

3.5 XDLVO analysis

The theoretical analysis of XDLVO was carried out on commercially available PVDF membranes and all modified membranes. The electron donor fraction (γ^-) of the MXene membranes increased significantly as compared to the pristine PVDF membranes, and increased with increase of loading (Table S1†), indicating the enhanced electron donor capacity of the MXene material.[56] After hydrothermal treatment, the surface γ^- values of TiO_2/MXene membranes further increased in comparison with PVDF membranes. The surface modification of MXene and TiO_2/MXene two-dimensional materials can enhance the negative charge on the membrane surface, hence improve the rejection of negatively-charged contaminants (due to the electrostatic repulsion) and increase their antifouling potential.[29]

To further understand the relationship between membrane fouling and foulant, the curves for each interaction energy *versus* the distance in the filtration process was plotted as shown in Fig. 7. Acid–base interactions dominate the total interfacial energy between the membrane and the foulant. The surface interaction energy with BSA was negative for all modified membranes, but the absolute values were significantly lower compared to the PVDF membranes and decreased with increasing load. These findings indicated that the commercially available PVDF membranes possess a stronger thermodynamic attraction to BSA as compared to the modified membranes.[57] Moreover, the MXene and TiO_2/MXene modifications reduce the potential for BSA and increase the resistance of the membrane material towards foulant. Overall, these results further suggested that the loading of MXene and TiO_2/MXene materials can significantly alleviate the membrane contamination problems caused by BSA adsorption to some extent.

4. Conclusion

In this study, TiO_2/MXene materials with strong photocatalytic properties and antibacterial ability were prepared by hydrothermal treatment of MXene lamellar materials. The presence of nano-TiO_2 on the MXene surface acted as an interlayer support column, improving the layer spacing and membrane flux. The best overall performance of the TiO_2/MXene membrane material was achieved at a loading of 3 mg (TM-0.24), with a BSA cut-off of 87.9% and a flux of 211.5 L m^{-2} h^{-1} bar^{-1}. Compared with the MXene membranes, the TiO_2/MXene membranes showed a significantly better self-cleaning performance after 6 h of UV irradiation, with FRR ranging from 60% to 79%. In addition, the TiO_2/MXene loading produced about >95% of *E. coli* inhibition, enhancing the antibacterial performance of the membrane. Furthermore, according to thermodynamic calculations, the loading of MXene and TiO_2/MXene reduced the interaction of BSA with the membrane surface and improved the antifouling performance. In conclusion, these results indicate that TiO_2/MXene membrane has a higher water throughput than commercially available ultrafiltration membranes and conventional MXene membranes, as well as strong self-cleaning and antimicrobial capabilities, which offer significant advantages in water and wastewater treatment processes.

Conflicts of interest

There are no conflicts to declare.

Acknowledgements

This work was financially supported by National Natural Science Foundation of China (52200015, 52000062).

References

1 S. F. Anis, R. Hashaikeh and N. Hilal, *Desalination*, 2019, **452**, 159–195.
2 H. T. Lay, R. J. E. Yeow, Y. Ma, A. L. Zydney, R. Wang and J. W. Chew, *J. Membr. Sci.*, 2021, **637**, 119589.
3 T. Yu, H. Sun, Z. Chen, Y. Wang, Z. Huo, N. Ikuno, K. Ishii, Y. Jin, H. Hu, Y. Wu and Y. Lu, *Sci. Total Environ.*, 2018, **644**, 486–493.
4 C. Li, W. Sun, Z. Lu, X. Ao and S. Li, *Water Res.*, 2020, **175**, 115674.
5 H. Rho, S. Im, O. Alrehaili, S. Lee, A. Jang, F. Perreault and P. Westerhoff, *Environ. Sci. Technol.*, 2021, **55**, 6984–6994.
6 A. J. Atkinson, M. D. Armstrong, J. T. Eskew and O. Coronell, *J. Membr. Sci.*, 2021, **629**, 119262.
7 S. Yuan, J. Li, J. Zhu, A. Volodine, J. Li, G. Zhang, P. Van Puyvelde and B. Van der Bruggen, *J. Membr. Sci.*, 2018, **563**, 655–663.
8 E. Igbinigun, Y. Fennell, R. Malaisamy, K. L. Jones and V. Morris, *J. Membr. Sci.*, 2016, **514**, 518–526.
9 N. Nasrollahi, L. Ghalamchi, V. Vatanpour and A. Khataee, *J. Ind. Eng. Chem.*, 2021, **93**, 101–116.
10 L. L. Coelho, M. Grao, T. Pomone, M. Ratova, P. Kelly, M. Wilhelm and R. D. F. P. Moreira, *Thin Solid Films*, 2022, **747**, 139143.
11 H. Zhang, A. U. Mane, X. Yang, Z. Xia, E. F. Barry, J. Luo, Y. Wan, J. W. Elam and S. B. Darling, *Adv. Funct. Mater.*, 2020, **30**, 2002847.
12 L. Zhang, Y. He, P. Luo, L. Ma, S. Li, Y. Nie, F. Zhong, Y. Wang and L. Chen, *Chem. Eng. J.*, 2022, **427**, 130948.
13 B. Xu and Y. Gogotsi, *Adv. Funct. Mater.*, 2020, **30**, 2007011.
14 J. Li, Q. Zhang, Y. Zou, Y. Cao, W. Cui, F. Dong and Y. Zhou, *J. Colloid Interface Sci.*, 2020, **575**, 443–451.
15 J. Li, X. Li and B. Van der Bruggen, *Environ. Sci.: Nano*, 2020, **7**, 1134–1289.
16 B. Xu and Y. Gogotsi, *Adv. Funct. Mater.*, 2020, **30**, 2007011.
17 V. Kamysbayev, A. S. Filatov, H. Hu, X. Rui, F. Lagunas, D. Wang, R. F. Klie and D. V. Talapin, *Science*, 2020, **369**, 979–983.
18 C. E. Ren, K. B. Hatzell, M. Alhabeb, Z. Ling, K. A. Mahmoud and Y. Gogotsi, *J. Phys. Chem. Lett.*, 2015, **6**, 4026–4031.
19 Q. Lin, G. Zeng, G. Yan, J. Luo, X. Cheng, Z. Zhao and H. Li, *Chem. Eng. J.*, 2022, **427**, 131668.
20 J. Zhang, L. Yang, H. Wang, G. Zhu, H. Wen, H. Feng, X. Sun, X. Guan, J. Wen and Y. Yao, *Inorg. Chem.*, 2019, **58**, 5414–5418.
21 H. Huang, Y. Song, N. Li, D. Chen, Q. Xu, H. Li, J. He and J. Lu, *Appl. Catal., B*, 2019, **251**, 154–161.
22 H. Song, Y. Wang, Z. Ling, D. Zu, Z. Li, Y. Shen and C. Li, *Sci. Total Environ.*, 2020, **746**, 141009.
23 H. Parse, I. M. Patil, A. S. Swami and B. A. Kakade, *ACS Appl. Nano Mater.*, 2021, **4**, 1094–1103.
24 T. Ke, S. Shen, K. Rajavel, K. Yang and D. Lin, *J. Hazard. Mater.*, 2021, **402**, 124066.
25 D. Xu, X. Zhu, X. Luo, Y. Guo, Y. Liu, L. Yang, X. Tang, G. Li and H. Liang, *Environ. Sci. Technol.*, 2021, **55**, 1270–1278.
26 J. Xu, Z. Wang, L. Yu, J. Wang and S. Wang, *J. Membr. Sci.*, 2013, **435**, 80–91.
27 R. P. Pandey, K. Rasool, V. E. Madhavan, B. Aïssa, Y. Gogotsi and K. A. Mahmoud, *J. Mater. Chem. A*, 2018, **6**, 3522–3533.
28 S. F. Anis, B. S. Lalia, M. Khair, R. Hashaikeh and N. Hilal, *Chem. Eng. J.*, 2021, **415**, 128395.
29 T. Lin, Z. Lu and W. Chen, *J. Membr. Sci.*, 2014, **461**, 49–58.
30 J. Liu, Y. Fan, Y. Sun, Z. Wang, D. Zhao, T. Li, B. Dong and C. Y. Tang, *J. Membr. Sci.*, 2021, **623**, 119048.
31 J. Li, S. Wang, Y. Du and W. Liao, *Ceram. Int.*, 2018, **44**, 7042–7046.
32 S. Tian, G. Cheng, Z. Tang, F. Sha, Z. Xuan and G. Ding, *Ceram. Int.*, 2020, **46**, 28949–28954.
33 C. Peng, H. Wang, H. Yu and F. Peng, *Mater. Res. Bull.*, 2017, **89**, 16–25.

34 T. Cai, L. Wang, Y. Liu, S. Zhang, W. Dong, H. Chen, X. Yi, J. Yuan, X. Xia, C. Liu and S. Luo, *Appl. Catal., B*, 2018, **239**, 545–554.

35 T. Liu, X. Liu, N. Graham, W. Yu and K. Sun, *J. Membr. Sci.*, 2020, **593**, 117431.

36 M. H. D. A. Farahani and V. Vatanpour, *Sep. Purif. Technol.*, 2018, **197**, 372–381.

37 L. Ding, Y. Wei, Y. Wang, H. Chen, J. Caro and H. Wang, *Angew. Chem., Int. Ed.*, 2017, **56**, 1825–1829.

38 K. Rasool, K. A. Mahmoud, D. J. Johnson, M. Helal, G. R. Berdiyorov and Y. Gogotsi, *Sci. Rep.*, 2017, **7**(1), 1–11.

39 C. Mao, X. Wang, W. Zhang, B. Hu and H. Deng, *Colloids Surf., A*, 2021, **614**, 126136.

40 Q. Zhong, G. Shi, Q. Sun, P. Mu and J. Li, *J. Membr. Sci.*, 2021, **640**, 119836.

41 A. Benito, G. Garcia and R. Gonzalez-Olmos, *J. Membr. Sci.*, 2017, **536**, 141–147.

42 L. Yang, D. Kan, C. Dall'Agnese, Y. Dall'Agnese, B. Wang, A. K. Jena, Y. Wei, G. Chen, X. Wang, Y. Gogotsi and T. Miyasaka, *J. Mater. Chem. A*, 2021, **9**, 5016–5025.

43 K. Huang, C. Li, H. Li, G. Ren, L. Wang, W. Wang and X. Meng, *ACS Appl. Nano Mater.*, 2020, **3**, 9581–9603.

44 W. Chen, P. Westerhoff, J. A. Leenheer and K. Booksh, *Environ. Sci. Technol.*, 2003, **37**, 5701–5710.

45 C. Wu, W. An, Z. Liu, J. Lin, Z. Qian and S. Xue, *J. Hazard. Mater.*, 2020, **390**, 121391.

46 X. Cheng, C. Hou, H. Gao, P. Li, X. Zhu, C. Luo, L. Zhang, Y. Jin, D. Wu and H. Liang, *Water Res.*, 2022, **211**, 118067.

47 K. Rajavel, S. Shen, T. Ke and D. Lin, *Appl. Surf. Sci.*, 2021, **538**, 148083.

48 W. Wang, H. Feng, J. Liu, M. Zhang, S. Liu, C. Feng and S. Chen, *Chem. Eng. J.*, 2020, **386**, 124116.

49 E. Park, J. Choi, Y. Park and K. Park, *Toxicology*, 2008, **245**, 90–100.

50 K. Rasool, M. Helal, A. Ali, C. E. Ren, Y. Gogotsi and K. A. Mahmoud, *ACS Nano*, 2016, **10**, 3674–3684.

51 S. Gurunathan, J. Woong Han, A. Abdal Daye, V. Eppakayala and J. Kim, *Int. J. Nanomed.*, 2012, 5901.

52 Y. Luan, S. Liu, M. Pihl, H. C. van der Mei, J. Liu, F. Hizal, C. Choi, H. Chen, Y. Ren and H. J. Busscher, *Curr. Opin. Colloid Interface Sci.*, 2018, **38**, 170–189.

53 T. Du, S. Chen, J. Zhang, T. Li, P. Li, J. Liu, X. Du and S. Wang, *Nanomaterials*, 2020, **10**, 1545.

54 H. M. Hegab, A. ElMekawy, L. Zou, D. Mulcahy, C. P. Saint and M. Ginic-Markovic, *Carbon*, 2016, **105**, 362–376.

55 K. Rasool, K. A. Mahmoud, D. J. Johnson, M. Helal, G. R. Berdiyorov and Y. Gogotsi, *Sci. Rep.*, 2017, **7**(1), 1–11.

56 Z. Huang, Q. Zeng, Y. Liu, Y. Xu, R. Li, H. Hong, L. Shen and H. Lin, *J. Membr. Sci.*, 2021, **640**, 119854.

57 Q. Wang, Y. Guo, Z. Wang, J. Zhang, J. Yao, L. Jiang and Z. Wu, *Water Environ. Res.*, 2021, **93**, 360–369.